LAWRENCE
LIVERMORE
NATIONAL
LABORATORY

UCRL-JRNL-203465

Supersonic propagation of ionization waves in an underdense, laser-produced plasma

C. Constantin, C.A. Back, K.B. Fournier, G. Gregori, S.H. Glenzer, M.C. Miller, E.L. Dewald, O.L. Landen

October 20, 2004

Physical Review Letters

Disclaimer

Supersonic propagation of ionization waves in an under-dense, laser-produced plasma

C. Constantin,* C.A. Back, K.B. Fournier, G. Gregori, O.L. Landen, S.H. Glenzer, and E.L. Dewald

Lawrence Livermore National Laboratory, 7000 East Avenue, Livermore, CA 94550

M.C. Miller

Los Alamos National Laboratory, Los Alamos, NM 87545

(Dated: October 20, 2004)

Abstract

We observe a laser-driven supersonic ionization wave heating a mm-scale plasma of sub-critical density up to 2-3 keV electron temperatures. Propagation velocities initially 10 times the sound speed were measured by means of time-resolved x-ray imaging diagnostics. The measured ionization wave trajectory is modeled analytically and by a 2D radiation-hydrodynamics code. The comparison to the modeling suggests that nonlocal heat transport effects may contribute to the attenuation of the heat wave propagation.

*Electronic address: constantin1@llnl.gov

I. INTRODUCTION

Studies of laser energy absorption in plasmas have great relevance for radiation hydrodynamics in astrophysical and laboratory plasmas, particularly for laser-driven inertial confinement fusion (ICF) research [1]. If the target material is underdense, meaning that the ionized electron density is lower than the laser critical density, the laser penetration depth can be on the order of many wavelengths, versus a fraction of a wavelength for solid foils. Once the underdense material is partially ionized by multiphoton processes, the rest of the laser energy is predominantly absorbed by saturable inverse Bremsstrahlung, creating an ionization wave [2]. The physics involved in the ionization wave propagation changes as the density of the target is lowered and the drive intensity increases. For example, if the ionization wave reaches the supersonic regime, the propagation of the ionization front is sufficiently fast that it outruns the hydrodynamic perturbations resulting from large pressure gradients between heated and unheated material and rarefaction waves arriving from the vacuum-sample interface. The resulting large volume heating of matter with little energy lost in hydrodynamic motion is an efficient mechanism for x-ray production, which makes underdense plasmas promising x-ray backlighting sources [3, 4]. Multi-keV x-ray sources are powerful tools for radiographing dense plasmas and investigating transient high-energy density related phenomena, which require brightness, uniformity and high photon energies over ns durations [5, 6]. The optimization of efficient backlighters depends not only on the development of new target materials, but on understanding the laser absorption, energy transport and coupling mechanisms in those materials as well.

Several investigations have been performed in the past to measure different regimes of ionization wave propagation that significantly change with plasma conditions. Hoarty *et al.* [7] measured an interesting transonic regime in 50 mg/cm^3 triacrylate foams irradiated with an intense pulse of soft x-rays and established that the transition from supersonic to subsonic propagation was caused by shocks preceding the ionization wave. The supersonic heat wave propagation reported in [8] in an underdense plasma (50 mg/cm^3 triacrylate foam), formed by intense thermal radiation fluxes was sustained for about 600 ps. After a steep increase to the maximum value of 3.5×10^7 cm/s, the front velocity smoothly decreases as target reemission starts to play a major role in the wave transport characteristics. Lower target densities (10 mg/cm^3 silica foam) were radiatively heated in [9] by a diffusive supersonic

wave that breaks out earlier than expected, due to energy losses to the target walls. In fused silica targets irradiated by ultrashort laser pulses of approximately 2 ps [10], the supersonic propagation of a radiation-driven ionization front was observed. The authors observe consistency of the front velocity with radiation driven thermal transport and discuss the transition from the electron conduction to radiation transport as the laser intensity increases from 10^{14} to 10^{17} W/cm^2. The closest conditions to our work in terms of target density and Iλ^2 (I is the laser intensity and λ is the laser wavelength) are those reported in the work of Koch *et al.* [11]. The targets are foams at much lower densities than the previously mentioned experiments (4-8 mg/cm^3) and the heat waves are driven by a 1 ns laser pulse with intensities in the range of 10^{14}-10^{16} W/cm^2. The time-resolved x-ray emission in the heat wave front shows a slower propagation than the theoretical predictions, and the reasons are not fully elucidated. Also, a disconnection from the laser pulse is observed, as the heat front velocity does not change when the laser turns off. According to the authors, the discrepancies between the data and the simulations indicate that possible anomalous absorption mechanisms need to be considered in the modeling of the data.

The novelty in the present work is that the laser at intensities above 10^{15} W/cm^2 irradiates initially solid targets at unprecedented low average densities relative to the critical density. Measuring the heat wave propagation in these new conditions and correlating it with the efficiency of the laser energy conversion into multi-keV x-rays (reported in [4]) is the primary goal of this experiment. The main questions that initiated our investigations were how fast can a heat wave propagate in these new, underdense materials, for how long can the supersonic regime be maintained before hydrodynamic motion effects occur and what is the x-ray production efficiency. Also, another interesting point was to compare the data with analytic models and with the radiation-hydrodynamic code LASNEX to understand the main factors influencing the energy transport in low-density laser-produced plasmas.

In the following section we will describe the laser configuration, the target geometry, and the diagnostic set-up. Section III describes the experimental results obtained from two time-resolved x-ray imaging diagnostics and presents a simple analytic model based on the formalism of Denavit and Phillion [2] in order to explain the heat wave trajectory. We present in section IV the numerical calculations employed for simulating this experiment, using the LASNEX code complemented by a hot-spot relaxation (HSR) model. This simplified 1D non-local transport model is introduced due to the difficulties encountered in modeling the

transport of the heat wave with the classical Spitzer-Härm formalism or flux-limited transport. Such non-local transport effects have been previously observed in similar plasmas characterized by large electron temperature gradients [11–14]. More sophisticated computational codes that solve Fokker-Planck equations and treat carefully the non-Maxwellian electron distribution function and electron collisions [15–18] are necessary to fully describe the transport problem and may constitute the subject of a theoretically oriented article. The last section in the present work concludes with our experimental observations and the comparison with the numerical simulations.

II. EXPERIMENTAL ARRANGEMENT

The samples to be heated were low-density silica aerogels doped with 3% Ti by atomic number, homogeneously distributed throughout the target, at initial densities of 3.1 and 3.3 mg/cm^3. These values correspond to electron densities in the ionized plasma of $\approx 0.1 n_{cr}$, where $n_{cr}=9\times10^{21}$ cm^{-3} is the critical density for the 3ω (351 nm) light. The aerogel is an open-cell foam with the cell size in the order of 50-100 nm, which makes it fairly uniform for the 351 nm laser light. The material was enclosed in an 80 μm thick Be cylinder of 2 mm diameter and 2.2 mm length.

We have carried out our experiment at the Laboratory for Laser Energetics (LLE) Rochester, using the OMEGA laser beams at 351 nm wavelength in flat-top pulses of 1.2 ns duration, with 150 ps rise and fall. Distributed polarization rotators (DPR) were installed to smooth the beams resulting in an instantaneous reduction of the speckle intensity by a factor of $\sqrt{2}$. The beams illuminate the target in three sets of beam cones at angles of 21.4° (cone 1), 42° (cone 2) and 58.9° (cone 3) relative to the cylinder axis, with 5, 5 and 10 beams per cone, respectively. All f/6.7 cone 1, 2 and 3 beams intersect at 300 μm before the target face and are defocused to produce a 400, 300 and 300 μm spot, respectively, at the target face normal to the beam axis. The spot size of the envelope of all beams measures approximately 1 mm in diameter on the target face. In this geometry, the incident energy was either 180 J/beam or 380 J/beam. For these two energies the target was heated from one side only, or both sides, with a total of 20 or 40 beams, respectively. To investigate the dependence of the laser energy transport on the incident irradiance, the average intensity onto the faces of the target were, correspondingly, 1.7×10^{15} and 3.4×10^{15} W/cm^2. The

laser configuration has a cylindrical symmetry and was meant to irradiate as much a target volume as possible (Figure 1).

To observe the heating of the aerogel an x-ray imaging streak camera was fielded at a near side-on view (11° to cylinder mid-plane) and filtered for the Ti He-like and H-like lines in the 4.7-5.5 keV range by using a 20 μm thick vanadium filter with 5.5 keV K-edge, that transmits 10-20% of incident signal intensity in this range. Calculated optical depths of $\tau < 0.04$ for He α indicate that the Ti lines are optically thin at these photon energies even if the whole 2 mm cylinder volume was emitting. The transmission through the Be walls of the aerogel enclosure was above 90%. The 250 μm wide streak slit of the detector was aligned parallel to the target axis, and the 1 mm long and 200 μm wide imaging slit was perpendicular to it. The time-resolution was 10 ps and the space resolution, achieved at a magnification of 10× was 220 μm.

Two-dimensional measurements complemented the heat-flow-propagation imaging by means of a gated x-ray framing camera (XRFC). This diagnostic viewed the target from 63.4° angle with respect to the target axis. We filtered the camera with 400 μm Be, which transmits more than 60% of the Ti K-shell emission. The target was imaged through 50 μm pinhole arrays onto four strips of a microchannel plate, each strip separated by 200 ps, with an exposure on each frame of approximately 80 ps. All images from the streak and framing camera were recorded onto photographic film and for each image the relative intensity was obtained by converting the film optical density into areal energy density (exposure) using calibration wedges exposed onto each film.

The fraction of the incident laser energy lost due to parametric instabilities such as stimulated Raman and Brillouin scattering (SRS and SBS) was measured by means of a full-aperture backscatter system (FABS). The signal scattered from the target back into the f/6.7 optics of a beam from the cone at 42° and a beam from the cone at 58.9° is measured simultaneously with a calorimeter and spectrally and temporally-resolved with a streak camera. The average is then multiplied by the total number of beams, with the assumption that the scattering of the beams at the lowest incidence angle (21.4°) can be described by the same averaged value measured in the beams incident at steeper angles. This assumption is reasonable in the conditions of a low level of backscatter signal, which was the case in our experiment.

III. RESULTS

A. X-ray imaging

Figure 2 shows a streak camera image of the heat waves propagating from the face toward the center of the target. The targets were illuminated from both sides (40 beams) with (a) 180 J/beam and (b) 380 J/beam. Figure 2(c) and (d) represent the heating of the target at the same energies as (a) and (b), correspondingly, from one side of the target only (20 beams). The time origin in these images was chosen as the time when the Ti emission is first observed. The heat front position is marked by the x-ray emission of Ti dopant in the aerogel, corresponding to the axial location where the material was heated to temperatures high enough for the Ti K-shell excitation. The positions in time were determined by scanning along the isointensity contours in each x-ray streak picture, up to the point where the two waves traveling in opposite directions interpenetrate as they reach the center of the target. The time of collision between the converging fronts at the center of the target varies with the input laser energy, i.e. it is 1.2 ns for the low energy case and 0.6 ns for the higher one. Position points were taken at 25% from the maximum intensity of the wave front, as well as at 10% and 45% and plotted together to analyze the maximum deviations that could occur during the scan of the contoured streak pictures. The measurement precision is generally better than 50 μm.

The heat front velocities for all experimental cases were calculated using a 3-point Lagrangian interpolation method to derive the position data points. The velocity curve is fitted by the derivative of the fit function for the position points and the error bars are calculated as the standard deviation of the derivative. By overlapping the velocity curves for each experimental case (Figure 3), we observed that, for the same laser energy, the velocities are consistent, independent to the type of irradiance (one- or two-sided). This fact demonstrates both the reproducibility of the experiment as well as the absence of any perturbation in the measured front due to the laser heating from the opposite direction. An increase of the velocity by a factor of $\approx$1.5 was observed when the laser energy is doubled. The maximum velocity value measured in the first 200 ps of the laser pulse is v=5.5 mm/ns at higher irradiances, and 3.75 mm/ns for the lower laser intensity case. After 800 ps, the heat wave has slowed down significantly and has asymptotically approached the calculated

sound speed, which was estimated as described in the Section III.B. to be c_s=0.3 mm/ns.

The lineouts superimposed on the streak images in Figure 2 (a) and (b) show the profile of the emission intensity at two times, before and after the wave interpenetration, i.e. t=0.3 and 1.5 ns, respectively. In the two-sided illumination cases, we observe a change of the maximum emission intensity by more than would result in the case of a simple radiation overlap on the detector. Based on the examination of the simulated density and pressure distributions, as well as the qualitative interpretation of the 2D framing camera images (Figure 4), it appears that compression was responsible for this increase in emissivity. In the one-sided illumination cases, where the material has one direction for relaxation toward the unheated part of the target, the compression is not as pronounced. To achieve a clear measurement of the heat wave propagation, our analysis extends to the point in time when hydrodynamic motion starts to play a role in the target material dynamics, which is close to the end of the laser pulse.

The velocity curves plotted in Figure 3 suggest that the propagation of the fronts decreases continuously and rather steeply in time, up to around 800 ps, after which it becomes more or less constant. Such behavior was also reported by other authors, either in transonic [7] or supersonic regimes [8], and the responsible mechanisms are either hydrodynamic motion catching up with the front at some point, or energy losses. In our case, the question was whether the trajectory is principally governed by the inverse Bremsstrahlung absorption of the diverging laser beams in the increasing volume of plasma, or are there additional losses such as transverse heat conduction that can play a major role at these high laser intensities. A simple model, based on the work of J. Denavit and D. Phillion [2] was employed to calculate the heat front propagation for the current case of an underdense target irradiated by a high-intensity, divergent beam, ignoring electron conduction or radiative losses (see Section III.C).

Figure 4 illustrates the 2D behavior of the heat waves and a global view on the volumetric target heating. The x-ray framing camera diagnostic was filtered for photon energies above 4.5 keV to observe the emission from the Ti dopant only. The times at which these frames are recorded give the possibility to inspect various aspects of the heat front radial and longitudinal expansion for all four experimental cases. Although an accurate quantitative measurement of the front velocity is inappropriate due to the angled orientation of the camera, the diagnostic proves useful in appreciating qualitatively the volumetric heating

process and the spatial evolution of the Ti emission. The frames in the row denoted (a) are the time-resolved x-ray images of the target irradiated at lower energy, from both sides. The detection starts at late times, after the laser pulse is turned off, and illustrates a heated target that emits from the entire volume. Noticeable is the occurrence of the collision of the opposing heat fronts at the center of the target by approximately 1.26 ns, in agreement with the indication of the streak camera image (Figure 2). Similar agreement is seen in the high energy case, displayed in sequence (b), where the waves traveling roughly by a factor of two faster meet earlier, at t=0.6 ns. In sequence (d), recorded for the low-energy case, 1-sided illumination, the expansion starts from the laser spot size on the target face (beams overlap over a 1 mm diameter region) up to the enclosure walls (about 2 mm) in approximately 0.65 ns. When the laser energy is doubled, the entire volume is radially filled by the Ti emission in about 0.40 ns, in sequence (c). In the two-sided illumination cases, the intensity increase on the center that we observed in Figure 2 is also observed in these images and suggests that the bright bulk emission at the center is a result of matter accumulation from all directions. The hydrodynamic motion is dominant close to or well after the laser pulse, depending on the input laser energy, causing a transition to a sonic propagation.

The levels of the backscattered light signal, measured with the FABS diagnostic were recorded for each case and indicate that the target only reflects 2.4-5% of the incident energy. These values were used to correct the measurement of the conversion efficiency (CE) of laser light to x-rays in the 4.5 to 5.5 keV photon energy range by an absolutely calibrated, time-integrated x-ray spectrometer [19]. The maximum value obtained for the 2-sided, higher-energy irradiation case was 2% of the absorbed laser energy. The line ratios from the spectrometer data also returned information on the plasma temperature, averaged over the pulse duration and entire volume. The measured values, T_e=2.25 keV for the low-energy shots and T_e= 3 keV for the high-energy cases, were in good agreement with numerical simulations. Details regarding the measurements and calculations of CE and temperature by spectroscopic means can be found in [4, 20].

B. Sound speed calculation

The sound speed was calculated adiabatically using a quotidian equation of state package (QEOS) [21]. The estimates for these targets were based on a collisional radiative (CR)

model that assumes a thermalized plasma with a Maxwellian electron distribution. The CR model employed hydrogenic atomic data for the O, Si and Ti ions, and the predicted rate of inverse Bremsstrahlung laser heating to compute the non-LTE ion populations. The plasma quickly reached an average charge Z=10, which was stable across a very wide range of temperatures. The CR model also showed that Ti 4.7 keV emission is strong from thermal plasmas with T_e >1.7 keV. Correlating an emission temperature of 1.7 keV with the heat wave front, the evaluation of the sound speed yielded c_s=0.3 mm/ns. In the hottest regions of the target, the sound speed reached a value of 0.41 mm/ns in the lower energy case and 0.46 mm/ns in the higher energy case. The sound speed calculation did not give different results when averaged over several cells (10-20, corresponding to 1 μm in the aerogel) versus one cell. Errors in this evaluation do not arise from the aerogel non-uniformities, as there are no large structures formed in the foam and the Ti-dopant is distributed homogeneously. The source of uncertainties is related to the assumption of a CR equilibrium and a Maxwellian electron distribution function.

C. Analytic modeling of heat wave trajectory

We have followed [2] and constructed an analytic model of the laser heating. The model, as applied in our case, assumes a stationary plasma with constant electron density, which is initially cold. The laser irradiation is modeled as a f/1.3 diverging beam, approximately matching the radially averaged power of 5 individual f/6.7 beams. These are the laser beams that comprise the lowest angle beam cone, which propagates further into the plasma than the other two cones. Since the diagnostic is viewing the front of the heat wave propagating along the target axis, it is expected that the heating from these beams is seen first. The pulse has a flat-top shape, with a 150 ps rise and fall, and a total of 1.2 ns duration, as in the experiment. We consider the 1-sided, higher-energy irradiation conditions, which is illustrated in Figure 6. The envelope of the individual f/6.7 beams of cone 1 represents a f/1.3 beam that has a 1 mm spot size at the target face and the focus at a distance of 1.3 mm away from the target face (Figure 5). The equation describing the intensity decay is:

$$\frac{1}{A}\frac{\partial(AI)}{\partial z} = -\frac{\kappa}{T_e^{3/2}}I \tag{1}$$

where A(z)=Cz_0^2 is the cross-section area of the laser beam at a distance z_0 from the virtual beam cone apex and focus and C=0.46 is a constant defining an f/1.3 divergence, I is the laser intensity, T_e is the plasma temperature and κ=7.2×10^5 $(eV)^{3/2}cm^{-1}$ is the absorption coefficient. For the calculation of κ we considered the Coulomb logarithm lnΛ=8 constant and the effective charge state, averaged over SiO_2 and Ti ions Z=10.

The temperature at the target face $T_{e0}(z = 0, t)$ is calculated using:

$$T_{e0}(t) = \left(\frac{5}{3}\frac{\kappa}{n_e k_B}\Phi_0\right)^{2/5} \tag{2}$$

with Φ_0 the incident laser fluence and k_B the Boltzmann constant. Then:

$$T_e(z,t) = \{(z_0/z)^{6/5}T_{e0}^{3/2} - \frac{15}{22}\kappa z[1-(z_0/z)^{11/5}]\}^{2/3} \tag{3}$$

calculates the plasma temperature profiles in time along the target axis, for a divergent beam with z_0=1.3 mm the distance from the virtual beam cone apex to target face. A plot illustrating the intensity of the laser, temperature profile along the target axis, and the velocity time-dependence is shown in Figure 6. In the first plot it is shown how the intensity profile attenuates inside the target from a maximum value at the target face due to absorption through inverse Bremsstrahlung.

The temperature at the target front location increases with the laser energy, and the plasma starts to radiate in the 4.7-5.5 keV band when the threshold temperature for the Ti K-shell emission is reached. At the boundary between heated and unheated material, the point on z axis where the temperature profile drops to zero determines the heat-wave-front location at a given time. This condition is written as T_e(z,t)=0 in Eq.3, from which it follows that the front position is:

$$z_{front} = z_0\left(\frac{T_{e0}^{3/2} + \frac{15}{22}\kappa z_0}{\frac{15}{22}\kappa}\right)^{5/6} \tag{4}$$

and the velocity can be obtained from the derivative of the front position in time.

We compared the analitically calculated front with the measured one in Figure 6 (bottom). The absolute timing of the data points was determined by accounting for a 200 ps ionization time before the first x-ray emission from the Ti can be observed. The ionization time is calculated using τ_i=1/$n_e S_Z$, where n_e is the electron density and S_Z is the ionization coefficient for creating an ion of charge Z. Figure 6 shows that the measured heat front

speed decreases more abruptly than the model while the laser pulse is on. Around t=200 ps the data points are higher than the modeled velocity of the front, due to the fact that the laser intensity analytically modeled is underestimated at the face of the target by distributing the intensity of the individual beams in cone 1 over a 1 mm area of the beam cone envelope. The steeper decrease of the data on the other hand can be explained by including other energy-loss mechanisms, such as energy transfer by electron conduction to the foam regions which the beams do not access directly and, in principle, radiative reemission from the energy deposition regions. The model ignores the energy into ionization processes, since the electron temperature is much greater than the average ionization potential.

D. LASNEX calculations

We have used LASNEX [22], a 2-D, Lagrangian, radiation-hydrodynamics code to simulate the heating of these targets. Ray-tracing techniques are used to track the laser propagation in the target, and laser energy is deposited by inverse Bremsstrahlung. The simulations were run with the average experimental energy per beam, delivered in a 1.2 ns square pulse with a 150 ps linear-ramp rise and fall. The electron conduction in the target is described by a multigroup flux-limited heat-diffusion model, considering in a given zone that the heat flux q=min($\kappa_{SH}\nabla$ T_e,f$v_e n_e T_e$), where κ_{SH} is the Spitzer-Härm thermal conductivity [23], ∇T_e the electron temperature gradient, f the flux limiter value, v_e the electron thermal speed, and n_e the electron density. We have varied the flux limiter in the simulations from 0.1 to 0.01, less inhibition to more, respectively. Both the electron heat conduction and radiation diffusion use a finite-element treatment, which gives a more accurate solution to the conduction equations for distorted Lagrangian meshes.

The experimental streaked x-ray images were compared with the simulated post-processed streaked x-ray images from all LASNEX runs. The calculated heat front positions are given by scanning along the isointensity contours in the post-processed simulated streak images at the 10%, 25%, and 45% levels of the signals, as in the data analysis. Best agreement was found for the case of 1.7×10^{15} W/cm^2 laser intensity and f =0.1 (Figure 7). However, discrepancies between the simulated and the measured propagation are observed after 300 ps, when the simulated heat wave starts to propagate faster than the observed fronts, in the higher-energy case.

There are several possible explanations for the inhibition of the heat wave that we observe in our plasma as compared to a heating characterized by a local thermal conduction model used in the LASNEX simulation: losses through parametric instabilities, magnetic field inhibition, or a nonlocal energy distribution. We consider the losses through parametric instabilities insignificant, since the measured fraction of light scattered due to stimulated Brillouin and Raman processes (SBS and SRS) in total are about 3% for the lower-energy case and 5% in the higher-energy case. Also, the magnetic fields in our plasma are weak, in the order of 0.088 MG, estimated using B[MG] $\approx 30(T_e)^{1/2}(1/L_T)(A/Z)^{1/2}$ [24], with B the magnetic field, A the atomic number, Z the average charge state and L_T the temperature gradient scale (all parameters calculated with LASNEX). We note that convective effects of the B-fields at the wall, observed in other studies [25], were neglected because the B-field production at the cylinder wall is small for low-Z targets. The radiative losses from the whole target in a band between 0.003 to 7 keV is on the order of 6×10^{11} W for the high-energy case, while for the low energy case is approximately 3×10^{11} W.

Due to the tight focusing of the laser beams onto the target, the temperature gradient scale length in our experiment becomes comparable with the electron-ion mean free path, which was calculated to be in the order of several hundred micrometers. For $\lambda_e \sim L_T$, where λ_e is the electron mean free path, it is known that nonlocal modeling becomes essential in improving the predictions of the classical energy transport calculations [26].

E. Hot-spot relaxation calculations

In order to estimate nonlocal effects on the heat transport relative to the LASNEX flux, we calculated the temperature profile using the hot-spot relaxation (HSR) model, a nonlocal nonlinear solver of the diffusion problem [27]. This technique was recently applied to analyze the temperature profile evolution in laser produced plasma relevant to ICF research [14]. We have used the LASNEX radial T_e profiles at t=300 ps and an axial position z=0.52 mm as initial conditions for the HSR problem. Such conditions are optimal for obtaining time dependent HSR T_e profiles outside the laser deposition region and in particular near the axis where the experimental data are taken. Around t=300 ps the first large discrepancies between the data and LASNEX predictions in the high-energy case are observed (see Figure 7), and the peak of the laser-energy deposition is at an axial coordinate z=0.52 mm but

radially far from the target axis. The HSR model calculates the evolution of the the initial LASNEX T_e profile for 50 ps and the result is compared to the LASNEX calculation at the same time (t=350 ps). The result was ΔT_e ~400 eV lower than predicted by LASNEX for the high energy case (T_e^{LASNEX} = 2.1 keV). Since the measurements of the heat wave rely on the Ti He_α emission measurement, which, according to the CR model and the LASNEX simulations, predominantly occurs above the T_e ≈1.7 keV, a reduction of 400 eV for the high energy case inhibits the He_α emission, which would be reflected in a delay of the flux-limited calculated heat wave propagation on the target axis. This corresponds to a shift in heat front position of about 60 μm, which reduces the velocity of the simulated heat front by a factor of 1.4. For the low energy case, the reduction in electron temperature was ~140 eV from T_e^{LASNEX}=1.85 keV and does not significantly modify the emission characteristics. For the same low-energy case, we compared the HSR results with LASNEX also at later times (t=800 ps) and the same location in a similar manner to the calculation done at t=350 ps. The HSR calculation starts from T_e^{LASNEX}= 1.75 keV. The temperatures resulting from the local (T_e^{LASNEX}=1.77 keV) versus nonlocal heat transport (T_e^{HSR}=1.72 keV) treatments differed by only 50 eV, showing a weaker influence of the nonlocal effects on the heat transport at the lower laser intensity. We conclude therefore that nonlocal effects are significant for laser intensities at or above few times 10^{15} W/cm^2, with a clearly increasing significance as the laser intensity rises.

IV. CONCLUSIONS

We have presented the results of an experimentally observed supersonic heat wave propagation in low-density Ti-doped aerogels irradiated at two laser intensities, 1.7×10^{15} W/cm^2 and 3.4×10^{15} W/cm^2. Our measurements show the temporal behavior of the heat fronts in a new material, at the lowest densities achieved in a solid target (≈3 mg/cm^3). We have demonstrated the possibility of heating large volumes of underdense material with a diverging supersonic heat wave generated by a direct multi-laser beam irradiation of the sample. We obtain an x-ray conversion efficiency in the 4.5-5 keV range (≈2% of the laser energy) comparable to the solid foils of pure Ti, but for a small fraction of Ti (3%). The laser energy is efficiently coupled to the plasma, with low fractions of incident light scattered due to parametric instabilities (2.5-5%). Comparisons to a simple analytic model including just

inverse Bremsstrahlung absorption for a diverging beam overestimate the heat-wave speed, suggesting that energy losses such as radiative re-emission and electron conduction are significant. Simulations including laser absorption and conduction, convective and radiative cooling performed using the LASNEX code show agreement with the heat-wave propagation data for a laser intensity of 1.7×10^{15} W/cm^2 but a faster propagation for the case of 3.4×10^{15} W/cm^2. The calculations considered a local electron conduction model based on flux-limited and Spitzer-Härm theory. By applying the HSR model that takes into account non-local effects of the energy transport and computes the evolution in time of the electron temperature profile, a stronger influence of the nonlocal electron conduction mainly in the higher intensity case was observed. This may lead to the conclusion that the experimental conditions fall into a transitory regime between local and nonlocal dominated electron heat transport. A more complex computational description of this problem, based on 2D non-local transport simulation with solutions from Fokker-Planck equations can be the subject of further studies to support these first insights.

We conclude that underdense foam targets are suitable platforms to study the laser energy deposition and heat transport, which are of general importance for high-laser intensity experiments and for benchmarking radiation-hydrodynamics codes. These also contribute greatly to the development of efficient x-ray backlighting sources, which are important in radiographing high-energy density and ICF-related phenomena.

V. ACKNOWLEDGEMENTS

This work was performed under the auspices of the U.S. Department of Energy by University of California Lawrence Livermore National Laboratory under contract No. W-7405-ENG-48. The authors would also like to thank to J. Poco, J. Satcher, C. Sorce, the Omega crew, and M. Primout for their support.

[1] J. Lindl et al., Phys. Plasmas **11**, 339 (2004)

[2] J. Denavit and D.W. Phillion, Phys. Plasmas **1**, 1971 (1994)

[3] C.A. Back et al., Phys. Plasmas **10**, 2047 (2003)

[4] K.B. Fournier et al., Phys. Rev. Lett. **92**, 165005-1 (2004)

[5] O.L. Landen et al., Re. Sci. Instrum. **72**, 627 (2001)

[6] S.G. Glendinning et al., Phys. Plasmas **6**, 3327 (2000)

[7] D. Hoarty et a, Phys. Plasmas **6**, 2171 (1994)

[8] T. Afshar-rad et al., Phys. Rev. Lett. **73**, 74 (1994)

[9] C.A. Back et al., Phys. Rev. Lett. **84**, 274 (2000)

[10] T. Ditmire et al., Phys. Rev. Lett. **77**, 498 (1996)

[11] J.A. Koch et al., Phys. Plasmas **2**, 3820 (1995)

[12] J.H. Rogers et al, Phys. Fluids B**1**, 741 (1989)

[13] D.S. Montgomery et al, Phys. Rev. Lett. **73**, 2055 (1994)

[14] G. Gregori et al., Phys. Rev. Lett **92**, 205006-1 (2004)

[15] S.H. Glenzer et al., Phys. Rev. Lett. **82**, 97 (1999)

[16] E. Fourkal et al., Phys. Plasmas **8**, 550 (2001)

[17] J.-P. Matte et al., Phys. Rev. Lett. **72**, 1208 (1994)

[18] E. Epperlein et al., Phys. Fluids B **3**, 3092 (1991)

[19] L.N. Koppel and J.D. Eckels, UCRL-79781 (1977)

[20] K.B. Fournier et al., Proc. SPIE Int. Soc. Opt. Eng. **5196**, 194 (2004)

[21] R.M. More et al., Phys. Fluids **31**, 3059 (1988)

[22] G. Zimmerman and W. Kruer, Comments Plasma Phys. Control. Fusion **2**, 85 (1975)

[23] L. Spitzer and R. Härm, Phys. Rev. **89**, 977 (1953)

[24] C.E. Max, *Laser-Plasma Interaction*, edited by R. Balian and J.C. Adam (North-Holland, Amsterdam, 1982)

[25] S.H. Glenzer et al., Phys. Plasmas **6**, 2117 (1999)

[26] A.V. Brantov, V.Y. Bychenkov, and W. Rozmus, Phys. Plasmas **8**,3558 (2001)

[27] O.V. Batishchev et al., Phys. Plasmas **9**, 2302 (2002)

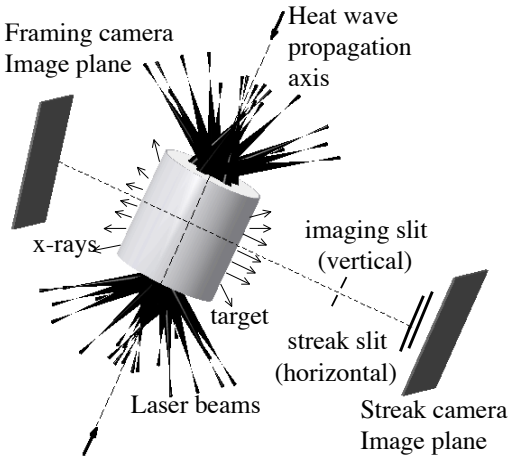

FIG. 1: A total of 40 laser beams illuminates the target in three cones (angles) from both sides, symmetrically. A x-ray streak camera with the slit aligned along the target axis was fielded for a near side-on view.

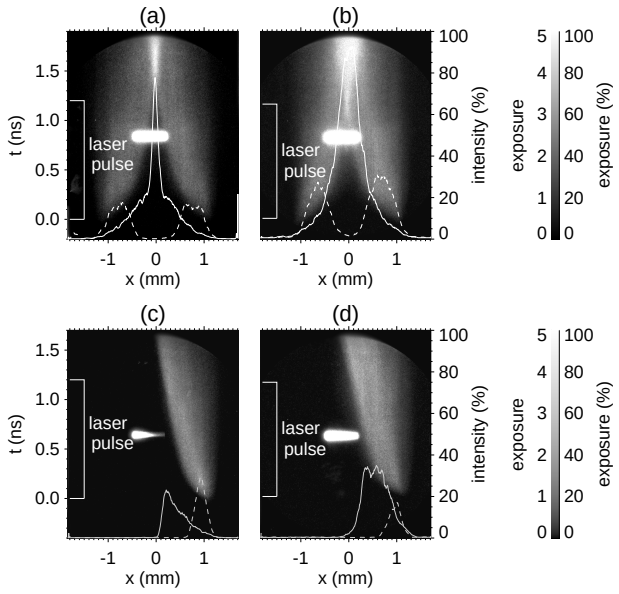

FIG. 2: Streak measurements in targets irradiated: (a) from both sides, at a laser energy of 7.2 kJ (180 J/beam); (b) from both sides, at 14.5 kJ (380 J/beam); (b) from one side, at 3.8 kJ; (d) from one side, at 7.6 kJ. The laser pulse is off after 1.2 ns. Lineouts at 0.3 ns after the laser pulse start (dotted line) and at 1.5 ns (solid line) are plotted in each picture. The intense rectangular spot in the center is caused by the x rays falling directly onto the phosphor screen of the streak camera. An intensity scale is mapped on the right-hand side.

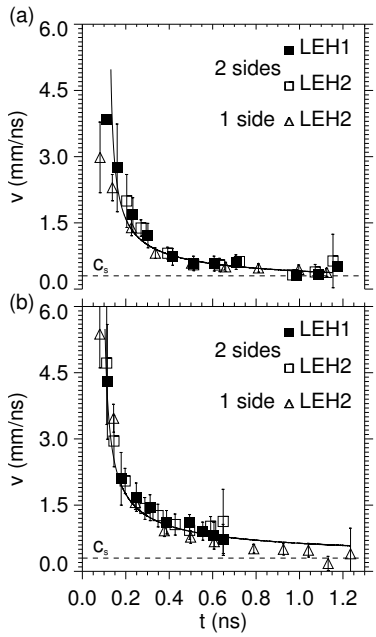

FIG. 3: Evolution of propagation velocity of the heat-wave front for two intensity cases: (a) 1.7×10^{15} W/cm^2 and (b) 3.4×10^{15} W/cm^2. The two-sided illumination data (denoted LEH1 and LEH2, with filled and empty squared symbols, respectively) are plotted together with the one-sided illumination data (LEH2, triangular symbols). The dashed line at 0.3 mm/ns represents the calculated sound speed in the plasma, c_s.

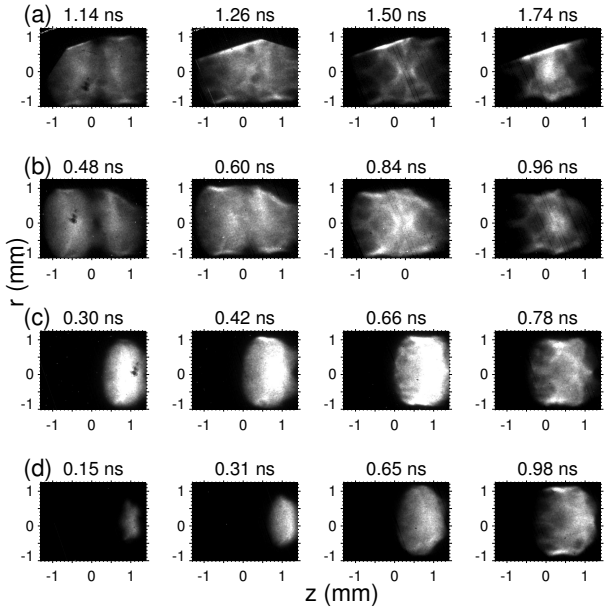

FIG. 4: A sequence of 2D x-ray images of the heated targets at different times, for each case: (a) two-sided, low-energy irradiation; (b) two-sided, high-energy irradiation; (c) one-sided, high-energy irradiation; (d) one-sided, low-energy irradiation. The heat wave expansion in time can be seen in both the target axis direction, z, and radially along the vertical axis, r.

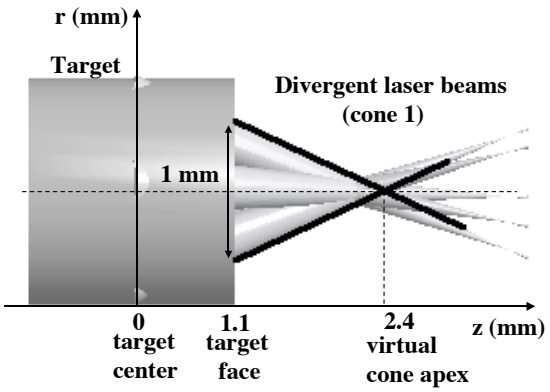

FIG. 5: The geometry of the plasma-laser system considered in the analytic model of the heat wave trajectory. In the model, the beam cone 1 (incident at 21.4° to the target axis) is approximated by a f/1.3 virtual cone (solid black line) with the apex at 1.3 mm away from the target face and a 1 mm spot size at the target face.

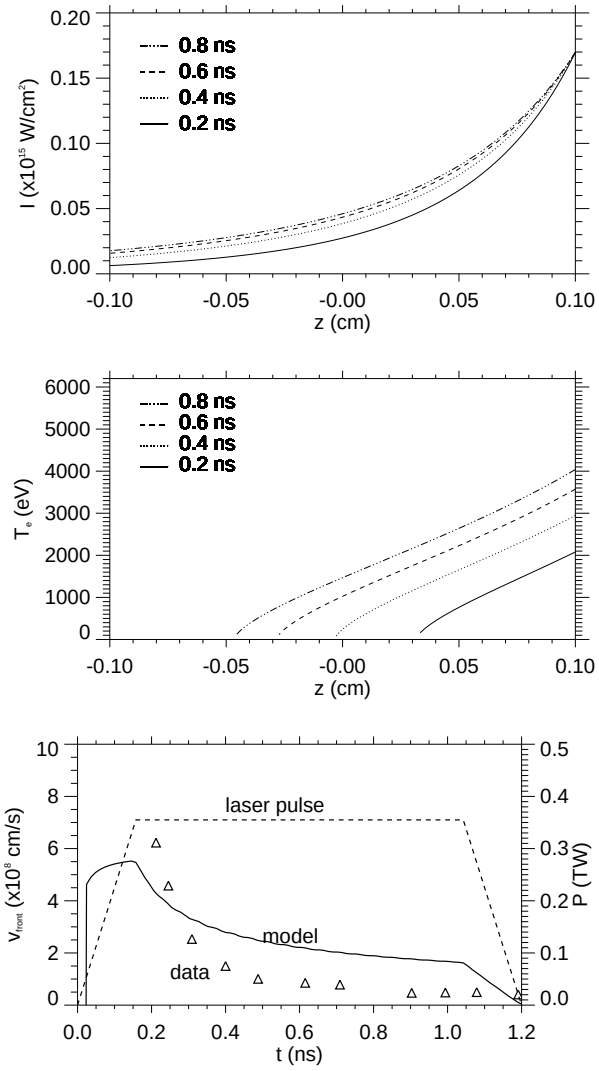

FIG. 6: The two upper plots are analytic calculations of the laser intensity and electron temperature profiles along the plasma axis at different times, for the high-energy case of the experiment. In these plots z=0 represents the target center and z=0.1 cm is the position of the irradiated target face. The lower plot shows the heat-wave-front velocity curve, calculated in the absence of any loss mechanisms (solid line) in comparison with the experimental case (triangular symbols).

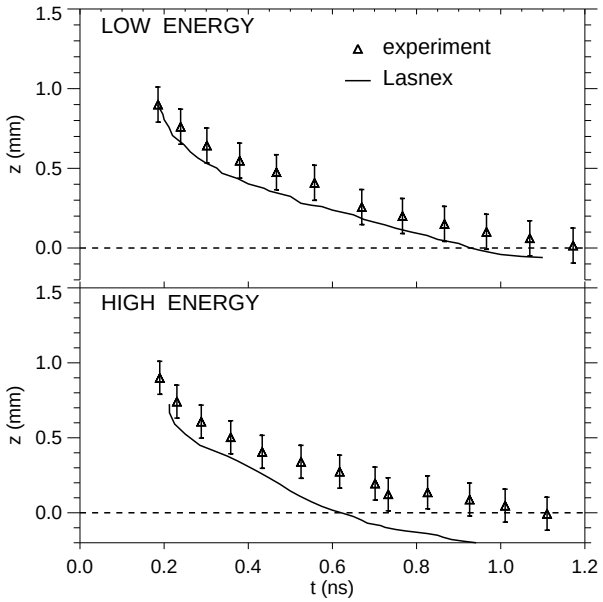

FIG. 7: The two plots show the comparison between the LASNEX calculations and the measured positions of the heat front in time. Inclusion of the HSR results (discussed in Section III.E.)will move the calculated curve up in the high-energy case. Illustrated are the low- and high-energy, 1-sided illumination shots, representative for the comparison. The 2-sided illumination shots are consistent with these cases for corresponding energies. The dotted line at 0 mm position indicates the target center.